Deliverable D3.1

Report on the nonlinear magnon population dynamics in vortex-based reservoirs

Project Number	101070290
Project name	Nonlinear Magnons for Reservoir Computing in Reciprocal Space
Project acronym	NIMFEIA
Work Package	WP3 Modelling the magnon reservoir in the GHz regime
Type	Report
Dissemination level	Public
Lead Beneficiary	UPS
Due date of delivery	Month 12 – September 2023

1. Summary

This report describes an application of the mode filtering technique for micromagnetics simulations that was outlined in Deliverable D3.4. Here, we discuss how the technique has been employed to estimate the population dynamics of spin-wave modes in a vortex state under different radio-frequency pulse sequences, which drive three-magnon scattering and cross-stimulation processes. The technique provides greater insight into the different scattering processes at play, which can only be surmised using conventional analyses of the power spectral density alone.

2. Background

At the core of the NIMFEIA project is the idea that reservoir computing can be performed using nonlinear magnon interactions within a modal multiplexing scheme. As discussed in Körber *et al*. [1], inputs involve binary AB sequences where each symbol 'A' and 'B' represents a radio-frequency field pulse, whose frequency closely matches one of the pure radial spin-wave eigenmodes n (with azimuthal number $m = 0$) about a vortex ground state. Outputs are constructed from the power spectral density (PSD) of the scattered spin-wave modes, where averages over frequency bins give the output vector.

Here, we seek to better understand the physical processes that underpin the reservoir functionality. Because the azimuthal spin-wave modes are similar to backward-volume modes, the dispersion relation $\omega(m)$ exhibits a sharp initial decrease before transitioning to a slower increase with m over a wide range of m, as shown in Fig. 1. This means that below the frequencies of the pure radial modes, specifically around half of these frequencies around which three-magnon processes occur, it is difficult to identify which scattered modes are involved based on analyses of the PSD alone. Moreover, we are interested in better understanding the transient processes involved with three-magnon scattering, in particular, cross-stimulation when two AB pulses overlap, which calls for a better time-resolved approach of the spin wave mode populations.

This report describes the use of the mode-filtering approach developed in the NIMFEIA project, as discussed in Deliverable D3.4, which allows us to project out the amplitudes of selected spin-wave eigenmodes $\psi_k(\mathbf{r}, t)$ on-the-fly as the magnetization dynamics is computed. Specifically, we use the MuMax3 open-source micromagnetics code [2] to perform a numerical time integration of the Landau-Lifshitz-Gilbert equation,

$$\frac{d\mathbf{m}_i}{dt} = -\gamma_0 \mathbf{m}_i \times \mathbf{H}_{\text{eff}} + \alpha \mathbf{m}_i \times \frac{d\mathbf{m}_i}{dt}, \tag{1}$$

where the normalized magnetization vector $\mathbf{m} = \mathbf{m}(\mathbf{r}, t)$ is solved self-consistently for each finite difference cell i. Here, γ_0 is the gyromagnetic constant, $\mathbf{H}_{\text{eff}}$ is the effective field which encompasses all short- and long-ranged magnetic interactions present at the site i, and α is the Gilbert damping constant. To lowest order, the fluctuations in the magnetization can be expanded in terms of the spin-wave eigenfunctions

$$\delta\mathbf{m}(\mathbf{r}, t) = \sum_k a_k(t)\psi_k(\mathbf{r}),$$

This project has received funding from the EU Research and Innovation Programme Horizon Europe under grant agreement No 101070290.

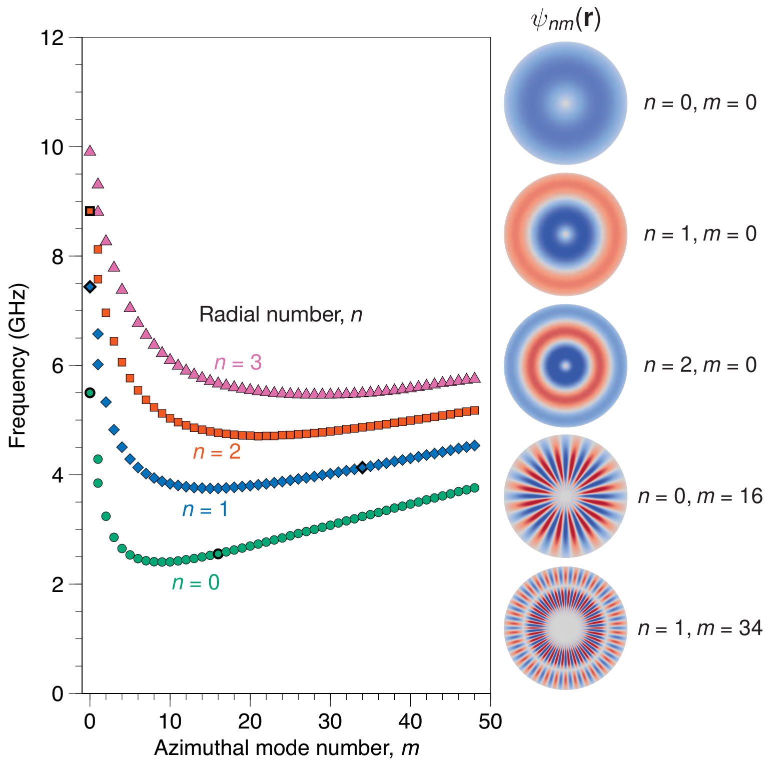

Figure 1. Dispersion relation of spin-wave eigenmodes in a 5-µm diameter, 50-nm thick permalloy disk computed using MuMax3 micromagnetics simulations. n is the radial number and m is the azimuthal number. The right panel shows the spatial profiles of a few eigenmodes, $\psi_{nm}(\mathbf{r})$, whose frequencies are indicated by symbols with thick edges.

where $a_k(t)$ are complex mode amplitudes, with the mode power being a measure of the mode population, $n_k \propto a_k^* a_k = |a_k|^2$. The module developed allows us to obtain $a_k(t)$ directly from the simulations for a given set of $\psi_k(\mathbf{r})$. Figure 1 illustrates the dispersion relation for the 5-µm diameter, 50-nm permalloy disk studied with a vortex configuration as the ground state, along with some eigenmode profiles.

3. Results

In order to illustrate the different transient dynamics at play, we focus here on different four-symbol AB sequences, as discussed in depth in Körber *et al*. [1]. Specifically, we will restrict our discussion to the input parameters $\nu_\mathrm{A} = 7.4$ GHz, $b_{\mathrm{rf,A}} = 3.5$ mT and $\nu_\mathrm{B} = 8.9$ GHz, $b_{\mathrm{rf,B}} = 3.0$ mT, where each symbol comprises a 20-ns pulse with a 5-ns overlap between successive pulses. By inspection from Fig. 1, these input frequencies correspond to the pure radial modes (1,0) and (2,0).

Figure 2 shows the population dynamics involving directly excited and scattered modes for the two baseline cases, 'AAAA' and 'BBBB'. In each case, the dynamics were computed for 100 different realizations of the random thermal field assuming a temperature of 300 K. The inclusion of thermal fluctuations means that we are dealing with a Langevin dynamics problem whereby each simulation run can result in quantitatively different dynamics, mimicking a realistic experimental scenario. In Fig. 2(a), the response of the directly-excited pure radial modes to the 'AAAA' sequence is shown. The dark, solid lines represent averages over the ensemble of 100 realizations, while the lighter lines in the background represent the different realizations for the (1,0) case. As expected, the (1,0) mode exhibits the greatest response to the 'AAAA' stimulus, where a steady state population is reached after a sharp transient response over a few ns. We also note that there is very little dispersion in the population dynamics over the different thermal realizations, which indicates that thermal activation only plays a small

This project has received funding from the EU Research and Innovation Programme Horizon Europe under grant agreement No 101070290.

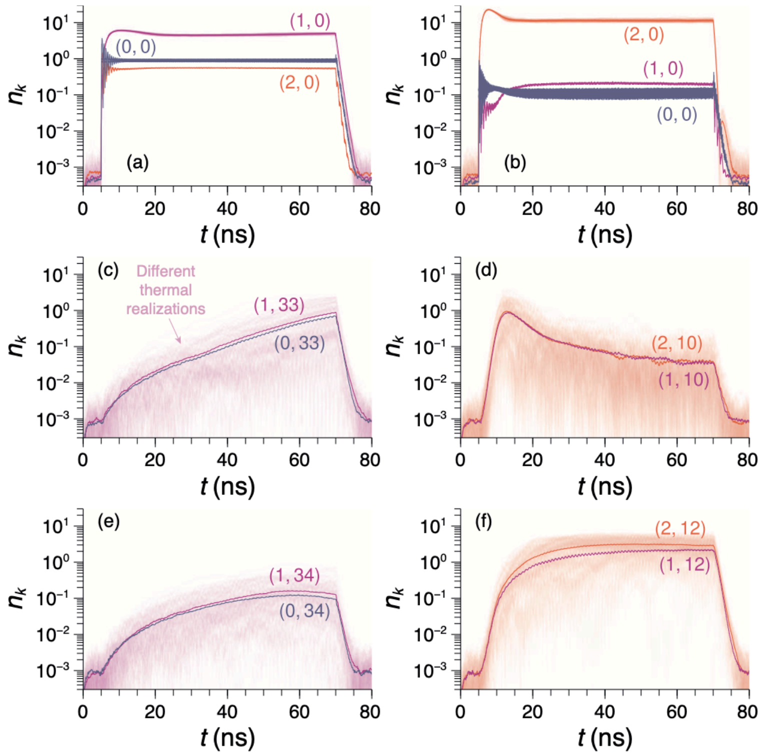

Figure 2. Population dynamics for selected (n, m) modes under 'AAAA' (a, c, e) and 'BBBB' (b, d, f) excitations, where $\nu_{\mathrm{A}} = 7.4$ GHz, $b_{\mathrm{rf,A}} = 3.5$ mT and $\nu_{\mathrm{B}} = 8.9$ GHz, $b_{\mathrm{rf,B}} = 3.0$ mT. Each pulse sequence lasts 20 ns, with a 5-ns overlap between sequences. Solid curves represent averages over 100 different realization of the random thermal fields. The curves are coloured according to the radial index, n.

role to direct excitation. Off-resonant excitation of the other pure radial modes, (0,0) and (2,0), can also be seen, where similarly to the (1,0) mode a large steady-state population a few orders of magnitude above thermal levels is attained after a sharp transient phase. Figure 2(b) shows similar behaviour in response to a 'BBBB' sequence, where instead it is the targeted (2,0) mode that reaches large steady state values, with the other radial modes (0,0) and (1,0) also exhibiting a strong response above thermal levels.

The population dynamics of the primary scattered modes are shown in Figs. 2(c)-2(f). For the 'AAAA' sequence, the main three-magnon scattering channels involve the $m = \pm 33{,}34$ modes on the $n = 0{,}1$ branches [Figs. 2(c) and 2(e)]. These modes exhibit growth from their thermal levels as soon as the directly-excited modes are driven out of thermal equilibrium. The $m = \pm 33$ modes grow at a near exponential rate throughout the duration of the 'AAAA' sequence, while the populations of the $m = \pm 34$ modes appear to saturate toward the end of the sequence. In contrast to the directly-excited modes, we can also observe a strong dispersion in the population dynamics of the scattered modes from one simulation to the next, which can be seen in the large spread of the light purple curves for the $n = 1$, $m = \pm 33{,}34$ modes in Figs. 2(c) and (e). For the 'BBBB' sequence, the onset of the scattered modes is also characterized by an exponential growth, however in one case ($m = \pm 10$) a gradual decrease in the population levels is observed after a maximum is reached [Fig. 2(d)], while for the other ($m = \pm 12$) the mode population saturates with time until the pulses are switched off. Like for the 'AAAA' case, the scattered modes also exhibit strong dispersion between the different thermal field realizations.

A broader view on these dynamics is given in Figs. 3 and 4, which illustrate the transient dynamics and the relationship between the different directly-excited and scattered modes involved with each of the 'AAAA' and 'BBBB' sequences. The idea of this representation is as follows. To schematize the population dynamics shown in Fig. 2, we use a series of circles to represent the time evolution of the mode population, where the radius of each circle is propor-

This project has received funding from the EU Research and Innovation Programme Horizon Europe under grant agreement No 101070290.

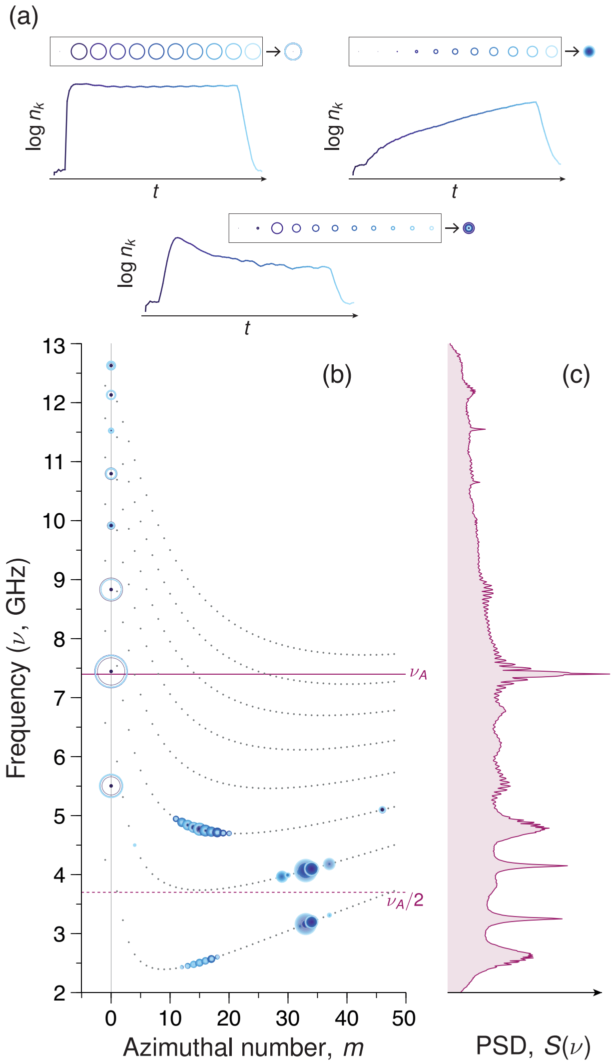

Figure 3. Population dynamics in response to an 'AAAA' input, where ν_A = 7.4 GHz, $b_\mathrm{rf,A}$ = 3.5 mT. (a) Schematic of the time dependence of mode population dynamics, condensed onto overlaid coloured circles. (b) Dispersion relation with coloured circles indicating directly-excited or scattered modes. (c) Power spectral density computed from the mode dynamics.

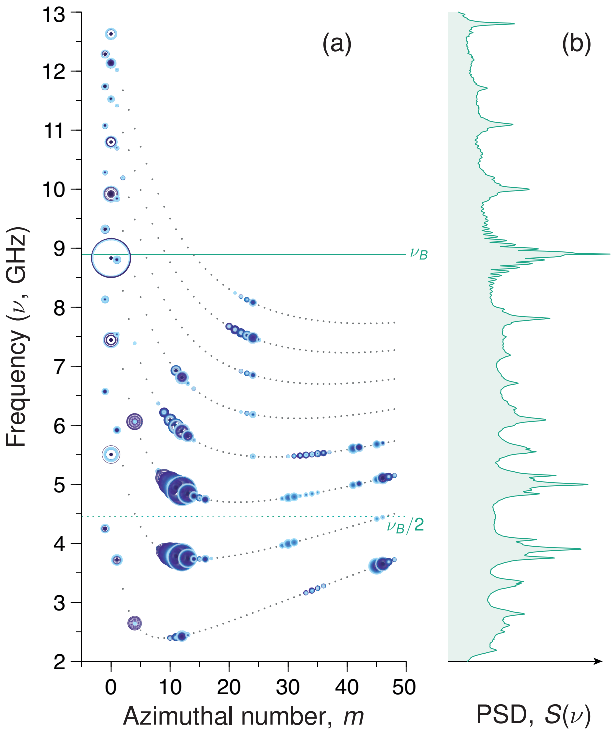

Figure 4. Population dynamics in response to a 'BBBB' input, where ν_B = 8.9 GHz, $b_\mathrm{rf,B}$ = 3.0 mT. (a) Dispersion relation with coloured circles indicating directly-excited or scattered modes. (b) Power spectral density computed from the mode dynamics.

tional to the mode population on a logarithmic scale at a given instant. Each circle is colour-coded from dark blue to light blue to indicate the direction of time. This scheme is illustrated in Fig. 3(a) for three different but representative behaviours of the mode population dynamics. The circles are then overlaid on top of one another to further condense the time evolution of the mode onto a point. Figure 3(b) shows the dispersion relation of the vortex eigenmodes, where modes excited either directly or indirectly by the 'AAAA' excitation are represented with the overlaid, coloured circles just described and all other modes are shown as small, gray dots. The positions of the excitation frequency, ν_A, and half its value are also indicated. This representation allows us to deduce at a glance the modes that are the most active under a given stimulus. As we mentioned earlier, the uniform rf field couples most strongly to the (1,0) mode, but we can deduce straightforwardly from this figure that all pure radial modes $m = 0$

This project has received funding from the EU Research and Innovation Programme Horizon Europe under grant agreement No 101070290.

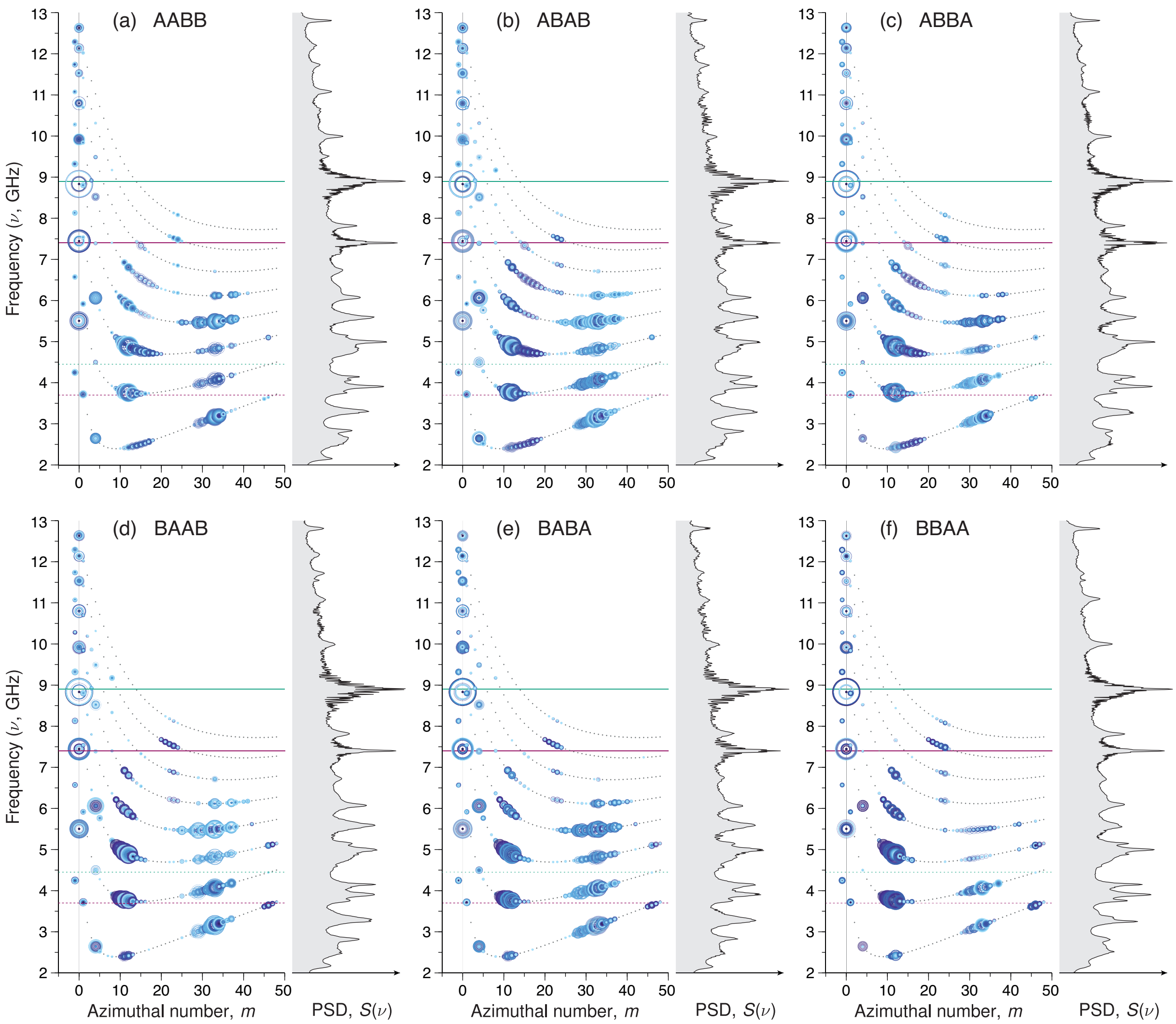

Figure 5. Population dynamics in response to four-symbol 'AB' sequences, with equal proportion of 'A' and 'B'.

studied are driven above their thermal levels. We can also see that the main channel for three-magnon scattering occurs around $m = 33{,}34$ as discussed previously, with a finite contribution also seen in the low and high 30s along with modes in between $m = 10$ and 20. As a point of comparison, the power spectral density of all the modes is shown in Fig. 3(c), where the scattered modes are represented by four dominant peaks around $\nu_A/2$. While frequency binning has been used successfully to construct the output space vectors for pattern recognition, knowledge of the individual mode populations may prove to be useful for processing more complex signals.

Figure 4 shows the response to a 'BBBB' excitation. In contrast to the 'AAAA' case, the main three-magnon scattering occurs for azimuthal indices $m = 10$ to 12, with a larger number of modes contributing from the $n = 1{,}2$ and $n = 0{,}3$ branches. We also see a significant contribution from modes $m > 30$. As expected, the corresponding PSD shown in Fig. 4(b) is much richer and features a greater number of well-defined peaks in the scattered mode spectrum, but again direct access to the mode population dynamics gives a more detailed view on the different scattering processes at play.

We now turn our attention to mixed 'AB' sequences, where cross-stimulation is conjectured to play a key role in the three-magnon scattering process [1]. Specifically, we compare the six

This project has received funding from the EU Research and Innovation Programme Horizon Europe under grant agreement No 101070290.

combinations of four-symbol 'AB' sequences in which there are two occurrences each of 'A' and 'B'. The corresponding population dynamics are shown in Fig. 5. As for the previous cases, the corresponding power spectral density of the spin-wave modes is also given. We can observe, qualitatively, certain features in the power spectrum that differ between the symbols, which is what allows us to use machine learning on the frequency-binned outputs to classify these different sequences [1]. Comparison with Figs. 3 and 4 also allows us to deduce that the mixed 'AB' sequences result in a greater number of modes that take part in the scattering processes across a broader range of azimuthal *and* radial numbers. For example, the primary 'BBBB' three-magnon response involving mainly $m = 10$ to 12 modes is extended across $m = 10$ to 20 for certain 'AB' combinations, such as AABB, ABAB, and ABBA. Similarly, the primary 'AAAA' three-magnon response involving mainly $m = 33{,}34$ is extended across $m =$ 28 to 38, which appears for almost all of the combinations considered. The greater number of modes excited is consistent with the appearance of new scattering channels when 'A' and 'B' pulses overlap.

Some examples of qualitatively different cross-stimulation processes are shown in Fig. 6 for three selected modes in response to 'ABAB' and 'BABA'. Schematics of the pulse sequence are shown in the inset at the top of the figure. Figures 6(a) and (b) illustrate the population dynamics of the (1,46) mode, which remains largely at thermal levels under 'AAAA' but is driven two orders of magnitude above thermal levels under 'BBBB' (as indicated by the grey curves). Under 'ABAB' [Fig. 6(a)], the presence of the existing 'A' pulse appears to inhibit the growth of the mode when the 'B' pulse is applied. The growth and decay profile of the mode varies between the two applications of the 'B' pulse, which reflects the short-term memory of the reservoir. A similar behaviour is observed for the 'BABA' sequence [Fig. 6(b)], where the initial growth driven by the 'B' pulse is inhibited as soon as the 'A' pulse is switched on. Again, a clear memory effect can be seen in the shape of the population profile.

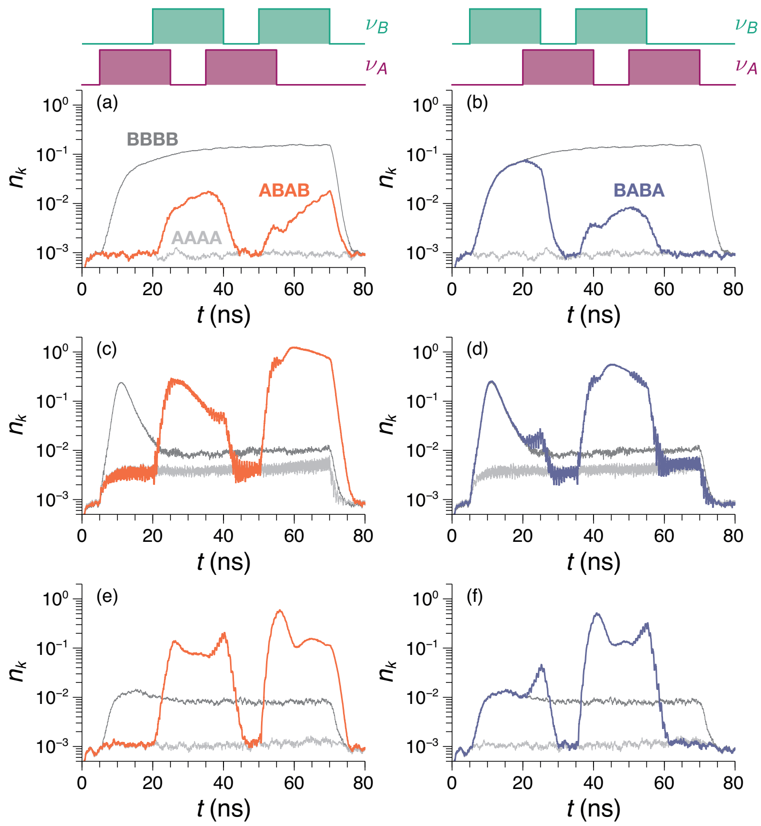

Figure 6. Population dynamics for selected (n, m) modes under ABAB (a, c, e) and BABA (b, d, f) excitations, where $\nu_{\mathrm{A}} = 7.4$ GHz, $b_{\mathrm{rf,A}} =$ 3.5 mT and $\nu_{\mathrm{B}} = 8.9$ GHz, $b_{\mathrm{rf,B}} =$ 3.0 mT. Each pulse lasts 20 ns, with a 5-ns overlap between pulses. (a,b) mode $(n, m) =$ (1,46), (c,d) mode (3,4), (e,f) mode (4,29). For comparison, the population dynamics for 'AAAA' and 'BBBB' sequences are shown in grey. Schematics of the pulse sequences are shown in the top inset.

This project has received funding from the EU Research and Innovation Programme Horizon Europe under grant agreement No 101070290.

An example of mode amplification is shown in Figs. 6(c) and (d) for the mode (3,4). This mode is driven above thermal levels under both ‘AAAA’ and ‘BBBB’, where steady state is gradually reached after some initial sharp transients. Under ‘ABAB’, the application of the ‘B’ pulse results in a sharp increase in the mode population, which is even larger after the second ‘B’ pulse. Similar amplification can also be seen for the reverse sequence [Fig. 6(d)]. For both sequences, we observe that the population levels return to the baseline set by the ‘A’ pulse dynamics when the ‘B’ pulse is switched off.

Finally, Figs. 6(e) and (f) for mode (4,29) illustrate how a largely dormant mode under an ‘AAAA’ excitation can stimulate strong scattering when combined with a ‘B’ pulse. Here, the mode remains close to thermal levels under ‘A’ alone, but provides an order-of-magnitude larger response for the ‘B’ pulse when it is applied. Again, strong non-commutativity and memory effects can be seen in the shape of the population profile.

4. References

1. L. Körber, C. Heins, T. Hula, J.-V. Kim, S. Thlang, H. Schultheiss, J. Fassbender, and K. Schultheiss, *Pattern recognition in reciprocal space with a magnon-scattering reservoir*, Nature Communications **14**, 3953 (2023).
2. A. Vansteenkiste, J. Leliaert, M. Dvornik, M. Helsen, F. García-Sánchez, and B. V. Waeyenberge, *The Design and Verification of MuMax3*, AIP Advances **4**, 107133 (2014).

This project has received funding from the EU Research and Innovation Programme Horizon Europe under grant agreement No 101070290.